RSC Advances

PAPER

View Article Online
View Journal | View Issue

Cite this: *RSC Adv.*, 2025, **15**, 38243

Effects of Cu and Zr Co-substitution on the structural, dielectric, and optical properties of $BiFeO_3$ ceramic

S. Zaidi, Z. Abdelkafi * and H. Khemakhem

Multiferroic materials, particularly $BiFeO_3$ (BFO) and its derivatives, have gained significant interest due to their potential applications in energy storage and photocatalysis. In this study, we investigate the effect of the low concentration (2%) of co-substitution with (Zr, Cu) on the structural, vibrational, optical, dielectric and ferroelectric properties of BFO. Both pristine BFO and $BiFe_{0.98}(Zr_{1/2}Cu_{1/2})_{0.02}O_3$ (BFCZ02) were synthesized through the solid-state reaction method. X-ray diffraction analysis revealed the good crystalline nature of both compositions, with the formation of impurities such as $Bi_{25}FeO_{39}$. Rietveld refinement and Raman analysis confirmed a consistent rhombohedral structure with the *R*3*c* space group for all samples. The average crystallite size decreased from 61.08 nm (BFO) to 39.08 nm (BFCZ02), indicating doping-induced grain refinement. Dielectric permittivity was studied over a wide temperature range (300–700 K) at various frequencies. An anomaly corresponding to the Néel temperature (T_N) was observed at 623 K for pure BFO, which decreased significantly to 604 K upon the co-substitution. A possible explanation for this shift was proposed. UV-visible spectroscopy at room temperature showed absorption peaks between 400 and 440 nm for both ceramics. The optical bandgap energy was estimated to be 2.34 eV for BFO and 2.21 eV for BFCZ02, suggesting the importance of the co-substitution of BFO in visible-light photocatalysis and photovoltaic applications. Possible reasons for the reduction in bandgap were proposed and discussed. The *P*–*E* loop study of the samples shows the modified ferroelectric behavior with Zr and Cu co-substitution. The results demonstrate that co-substitution with Zr and Cu enhances the optical response, improves dielectric performance, positioning BFCZ-02 as a promising candidate for multifunctional applications, including photovoltaics, photocatalysis, energy harvesting, and adaptive dielectric devices.

Received 24th April 2025
Accepted 2nd October 2025

DOI: 10.1039/d5ra02877a

rsc.li/rsc-advances

1 Introduction

The most well-known multiferroic material, $BiFeO_3$ (BFO), has attracted considerable attention in recent decades due to its unique coupling of ferroelectric, magnetic, and elastic order parameters, positioning it as a promising candidate for multifunctional devices in spintronics, data storage, and energy conversion systems.[1,2] BFO exhibits an antiferromagnetic Néel temperature (T_N) of approximately 350–370 °C,[3] and a ferroelectric Curie temperature (T_C) exceeding 800 °C.[4,5] Such high transition temperatures make BFO a strong candidate for exhibiting a magnetoelectric effect even at room temperature (RT). However, bulk BFO exhibits an incommensurate spin cycloid ($\lambda_0 \approx 62$ nm), which largely suppresses weak ferromagnetism and the linear magnetoelectric (ME) effect. In addition, synthesizing phase-pure BFO remains a challenge due to the frequent formation of secondary phases such as $Bi_2Fe_4O_9$ and $Bi_{25}FeO_{39}$, which arise from the volatility of bismuth at high temperatures, as well as the presence of oxygen vacancies and mixed valence states of Fe ions (Fe^{2+}/Fe^{3+}). These issues lead to increased leakage currents and electrical conductivity, thereby degrading the material's dielectric and ferroelectric performances and limiting its practical applications.[6] Chemical substitution is among the most effective strategies to address these challenges. For instance, substituting Fe^{3+} with Zr^{4+} has been shown to enhance both the electrical and magnetic properties of BFO.[7,8] Moreover, several studies have reported that the substitution of Fe^{3+} sites with Ti^{4+} and Zr^{4+} improves the multiferroic behavior of BFO.[9,10] Additionally, doping the Fe site with transition metals such as Cu^{2+} has also been found to enhance the magnetic and electrical properties of BFO.[11] Notably, BFO has demonstrated significant potential in photovoltaic and photocatalytic applications, owing to its ability to convert the solar energy into electrical energy and its intrinsic photocatalytic activity. To further broaden the light absorption spectrum of BFO and enhance its solar energy conversion efficiency, reducing its bandgap energy (E_g) is essential. Doping is also a potential

Laboratory of Multifunctional Materials and Applications (LaMMA), LR16ES18, Faculty of Sciences of Sfax, University of Sfax, B.P. 1171, Sfax, 3000, Tunisia. E-mail: zied_abdelkafi@yahoo.fr

method to reduce the E_g of BFO. Several previous studies have found that doping with the 4+ ion,[12] as well as doping with the 2+ ion,[13] has led to a remarkable reduction in the E_g of BFO. Motivated by these findings, our study focuses on the effect of co-substituting Cu^{2+} and Zr^{4+} ions for Fe^{3+} on the structural, vibrational, dielectric, optical, and ferroelectric properties of BFO. Specifically, we investigate two ceramics from the $BiFe_{1-x}(Cu_{1/2}Zr_{1/2})_xO_3$ system, with $x = 0$ (BFO) and $x = 0.02$ (BFZC02), synthesized *via* the solid-state reaction method. Structural characterization will be carried out using X-ray diffraction (XRD) to assess phase purity and determine cell parameters. Raman spectroscopy measurements will be employed to elucidate local structural variations as a function of the substitution rate. The dielectric behavior will be examined using impedance spectroscopy, providing insights into the dielectric response. Optical properties will be analyzed through UV-visible spectroscopy to evaluate the effect of doping on the band gap energy. Additionally, polarization–electric field (*P*–*E*) hysteresis loop measurements will be performed to further explore the ferroelectric properties of the materials.

2 Experimental procedure

BFO and BFZC02 ceramics were successfully prepared using the solid-state reaction method. In a typical procedure, Bi_2O_3, Fe_2O_3, ZrO_2, and CuO powders (each with a purity greater than 99%) were first dried in an oven at 200 °C for 12 h. The dried powders were then weighed according to the stoichiometric ratios specified in the following chemical reaction:

$$\frac{1}{2}Bi_2O_3 + \frac{(1-x)}{2}Fe_2O_3 + \frac{x}{2}CuO + \frac{x}{2}ZrO_2 \rightarrow BiFe_{1-x}\left(Cu_{1/2}Zr_{1/2}\right)_xO_3$$

Here, a 5 mol% excess of Bi_2O_3 was added to compensate for bismuth volatilization during the heat treatment. Based on the selected precursor ratios, the synthesis strongly favors the substitution of Zr^{4+} (0.86 Å, CN = 6) and Cu^{2+} (0.87 Å, CN = 6) into the Fe^{3+} site (0.69 Å, CN = 6), as both cations adopt octahedral coordination compatible with the B-site environment.[14] Moreover, the co-doping of Zr^{4+} and Cu^{2+} establishes a charge compensation mechanism with Fe^{3+} ($Fe^{3+} \leftrightarrow Zr^{4+}/Cu^{2+}$), which suppresses excess oxygen vacancies and enhances the structural stability of the perovskite lattice.

Using an agate mortar, the powder was mixed and ground for 2 h to ensure homogeneity. Subsequently, under a uniaxial pressure of 100 MPa for about 5 min, the milled powder was pressed into a disc with a diameter of 13 mm and a thickness of 10 mm. The obtained pellet was calcined at 600 °C for 2 h as the first calcination. Afterward, the calcined pellet was ground once again during 2 h to homogenize the powder and reduce the grain size. The powder was then subjected to a second calcination at 700 °C for 2 h to achieve the desired phase. After this stage, the pellet was ground for 1 h and then pressed under 100 MPa into a disk shape with a thickness of about 1.5 mm and a diameter of 8 mm. Finally, the compacted pellets were sintered at 900 °C for 3 h.

The phase purity and crystal structure of BFO and BFZC02 ceramics were anaysed using X-ray diffraction (XRD) at RT. The XRD data were collected using an X'Pert Panalytical diffractometer equipped with a cobalt target ($\lambda = 1.7889$ Å) in the 2θ range of 15° to 80° with a step size of 0.0167°. The crystalline phases and cell parameters were examined, and the crystallite sizes were determined from the full width at half maximum (FWHM) of the diffraction peaks using the Scherrer equation. Raman spectra were recorded for all samples using a Horiba Jobin-Yvon (HR 800UV) micro-Raman spectrometer with a 532 nm excitation wavelength. All measurements were performed at RT over the wavenumber range of 50–800 cm^{-1}. Dielectric measurements were conducted on gold-coated pellets over a temperature range of 300–700 K and at various frequencies (100 kHz to 1 MHz), using an automatic impedance analyzer (HP 4284A). UV-vis absorption spectra were recorded in the wavelength range 400–800 nm in order to estimate the bandgap using a UV-3600 Spectrophotometer (SHIMADZU, Japan) at RT. The ferroelectric hysteresis loops were recorded using an oscilloscope (Metrix OX 6062-II) in a homemade Sawyer–Tower circuit connected to a function generator (Metrix GX 320) and a high voltage amplifier (Matsusada AMS-5b6-L) at a frequency of 15 Hz at RT.

3 Results and discussion

3.1 X-ray diffraction analysis

Fig. 1(a) and (b) present the experimental XRD patterns of the BFO and BFZC02 ceramics (red circles). The diffraction patterns exhibit sharp and intense peaks, indicating good crystallinity and phase purity of the synthesized compounds. However, a minor secondary phase was detected in all ceramics. Based on previous studies on BFO-based materials,[15,16] this impurity phase has been identified as $Bi_{25}FeO_{39}$, which is commonly observed in BFO ceramics due to the volatility of bismuth, especially at high temperatures.

To further investigate the structural properties, Rietveld refinement was performed using the FullProf software package with WinPLOTR.[17] This method adjusts the calculated diffraction pattern to match the experimental one, enabling precise determination of the crystal structure, cell parameters, interatomic distances (Bi–O), atomic positions (Bi/Ba, Fe/Zr/Cu), and bond angles (Fe–O–Fe) of the synthesized materials. Additionally, this refinement allowed us to quantify the $Bi_{25}FeO_{39}$ impurity phase present in each composition.

The Rietveld refinement results (Fig. 1) confirm that both BFO and BFZC02 ceramics adopt a rhombohedral structure with an *R3c* space group. This indicates that the co-substitution of Fe^{3+} by Zr^{4+} and Cu^{2+} at a 2% doping level does not alter the fundamental structure of BFO. The detailed parameters extracted from Rietveld refinement for both ceramics are summarized in Table 1. For example, Fig. 2 illustrates the crystal structure of BFZC02, generated using refined ionic positions obtained from Rietveld refinement with the VESTA software. The analysis reveals that co-substitution with Zr^{4+} and Cu^{2+} leads to an increase in cell parameters, resulting in an expansion of the unit cell volume. This expansion is attributed

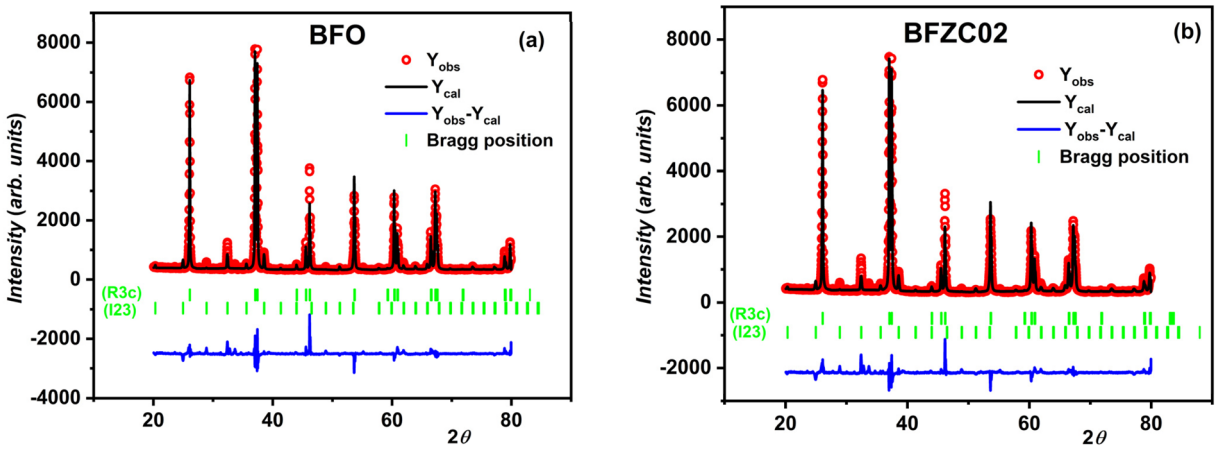

Fig. 1 Recorded and calculated X-ray diffractograms for BFO (a) and BFZC02 (b) ceramics at RT.

Table 1 Rietveld refinement results of the X-ray diffractograms for BFO and BFZC02 ceramics

	Space group	Cell parameters (Å)	Atomic positions	x	y	z	Occ	Interatomic distances (Å)	Bond angle (deg.)
BFO	$R3c$ (97.49%)	$a = b = 5.5786$	Bi (6a)	0.0000	0.0000	0.0000	0.3333	Bi–O = 2.549	Fe–O–Fe 155.82
		$c = 13.8678$	Fe (6a)	0.0000	0.0000	0.2191	0.3333	$Fe–O_1 = 1.981$	
		$V = 373.756$	O (18b)	0.4503	0.0227	0.9495	1.0000	$Fe–O_2 = 2.073$	
$Bi_{25}FeO_{39}$	$I23$ (2.51%)								
BFZC02	$R3c$ (97.82%)	$a = b = 5.5814$	Bi (6a)	0.0000	0.0000	0.0000	0.3333	Bi–O = 2.550	Fe–O–Fe 155.80
		$c = 13.8778$	Fe (6a)	0.0000	0.0000	0.2166	0.3266	$Fe–O_1 = 1.984$	
		$V = 374.405$	Zr/Cu (6a)	0.0000	0.0000	0.2166	0.0033	$Fe–O_2 = 2.073$	
			O (18b)	0.4550	0.0229	0.9498	1.0000		
$Bi_{25}FeO_{39}$	$I23$ (2.18%)								

to the larger ionic radii of Zr^{4+} (0.86 Å) and Cu^{2+} (0.87 Å) compared to Fe^{3+} (0.69 Å). Despite this increase in volume, the Fe–O–Fe bond angles remain practically unchanged, and the presence of the $Bi_{25}FeO_{39}$ impurity phase is relatively reduced.

The XRD patterns were also employed to estimate the average crystallite size (D), microstrain (ε), and dislocation density (δ) of the BFO and BFZC02 samples. The crystallite size (D) was determined using the Debye–Scherrer equation, as given below:[18]

$$D = \frac{k\lambda}{\beta \cos(\theta)} \quad (1)$$

where k is the shape factor which is about 0.89, λ denotes the wavelength of the X-rays (CoKα, $\lambda = 1.7889$ Å), β represents the full width at half maximum (FWHM) in radians and θ is the Bragg's angle in degrees. Moreover, the microstrain ε is estimated by using the following equation:[19]

$$\varepsilon = \frac{\beta}{4\tan\ \theta} \quad (2)$$

In addition, the dislocation density (δ), which provides insight into the crystalline quality of the samples, is calculated using the following relation:[20]

$$\delta = \frac{1}{D^2} \quad (3)$$

Table 2 summarizes the calculated parameters: D, ε, and δ for both BFO and BFZC02. For these compositions, the average crystallite size values confirm the nanocrystalline nature of the synthesized ceramics. A noticeable decrease in crystallite size is

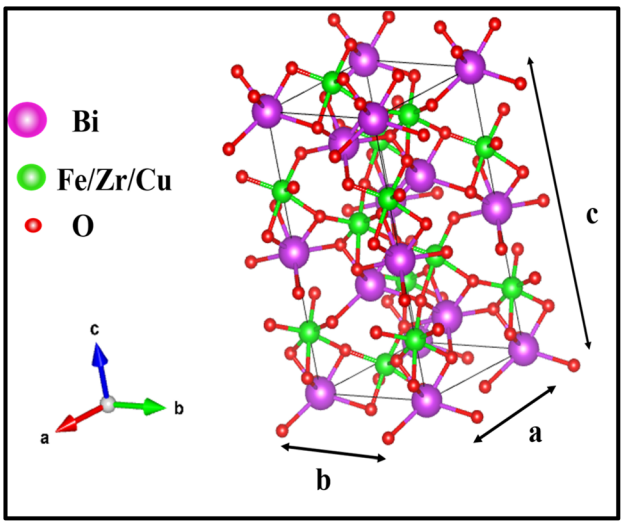

Fig. 2 Crystalline structure of BFZC02 generated using Vesta software.

Table 2 Microstructural parameters of the BFO and BFZC02

Sample name	Cristallite size D (nm)	Microstrain ε (10^{-3})	Dislocation density δ (10^{-3} nm^{-2})
BFO	61.08 ± 1.95	1.92 ± 0.06	0.27 ± 0.02
BFZC02	39.08 ± 3.13	3.22 ± 0.21	0.65 ± 0.10

observed, from 61.08 nm in BFO to 39.08 nm in BFZC02, following a 2% co-substitution of Fe by Cu and Zr. This reduced in crystallite size is also observed in Cr doped BFO system at Fe site.[21] In the present case, the suppression of oxygen vacancies likely contributes to this reduction in D. Oxygen vacancy concentration is known to govern grain growth, as it directly influences ion diffusion rates during crystallite agglomeration and grain formation processes.[22] Concurrently, the observed increase in δ reflects a decline in crystalline order, while the rise in ε suggests the formation of denser, more compact crystallites in the doped BFO.

3.2 Raman study

Fig. 3a displays the Raman spectra in the range of 50–800 cm^{-1} for BFO and BFZC02 compositions at RT. The spectra suggest that the substitution of Fe^{3+} by Zr^{4+} and Cu^{2+} does not alter the crystalline structure of the parent BFO, as confirmed by XRD analysis. Both ceramics retain the rhombohedral *R3c* symmetry, which is associated with 13 optical phonon-active modes ($4A_1$ + 9E).[23,24] The A_1 and E modes are Raman and infrared active, respectively.[25] The exact Raman peak positions were obtained by fitting the measured BFO spectrum followed by deconvolution of the fitted curve. The different modes identified through this fitting (E_{-1}, A_{1-1}, A_{1-2}, A_{1-3}, E_{-3}, E_{-4}, E_{-6}, A_{1-4} and E_{-7}) are indicated in Fig. 3b following the assignment by Pani *et al.*[26] In the higher wave-length range, certain modes such as E_{-5}, E_{-8} and E_{-9} are very difficult to distinguish. This is likely owing to the weak polarizability or the overlapping of narrowly spaced Raman vibrations.[27] According to Hermet et *al.*,[28] Bi atoms contribute primarily to low-frequency modes (up to 167 cm^{-1}), while oxygen vibrations dominate above 262 cm^{-1}. Fe atoms contribute mainly in the 152–262 cm^{-1} range, with possible involvement in higher-frequency modes. As shown by the dashed lines in Fig. 3a, the positions of the A_{1-1}, A_{1-2}, and A_{1-3} modes in BFZC02 remain unchanged compared to pure BFO. This indicates that the substituent elements predominantly occupy the Fe sites (B-site), leaving the A-site (Bi) environment unaffected. A similar observation was reported in the $BaFe_{1-x}Zr_xO_3$ system.[29]

3.3 Dielectric measurements

Fig. 4(a) and (b) depict the temperature-dependent dielectric constant (ε_r') and tangent loss (tan δ) (inset) of the BFO and BFZC02 ceramics, respectively, measured over the frequency range of 100 kHz to 1 MHz. For both BFO and BFZC02, as the temperature increases, ε_r' gradually rises, reaches an obvious maximum, and then decreases, regardless of the frequency. This maximum corresponds to the phase transition from the antiferromagnetic to the paramagnetic phase, which occurs at the Néel temperature (T_N). Here, T_N value decreases from 623 K for pure BFO to 604 K for BFZC02. While several studies attributed such the reduction T_N[7,30,31] in substituted BFO to a decrease in the Fe–O–Fe bond angle (θ), linked to T_N *via* the relation:[32]

$$T_N = JZS(S + 1)\cos\theta \quad (4)$$

(where J is the exchange constant, Z is the coordination number, and S is the spin of Fe^{3+}), XRD analysis reveals that θ remains almost unchanged in Zr/Cu co-substituted BFO. Instead, the T_N reduction likely stems from weaker magnetic interactions caused by substituting Fe^{3+} ions (0.69 Å) at the B-site with larger Cu^{2+} (0.87 Å) and Zr^{4+} (0.86 Å) ions. Consequently, the co-substitution creates a distribution of weaker exchange constants (J_{Fe-Zr}, $J_{Fe-Cu} < J_{Fe-Fe}$), lowering the overall magnetic interaction strength J. As a result, the weakening of J

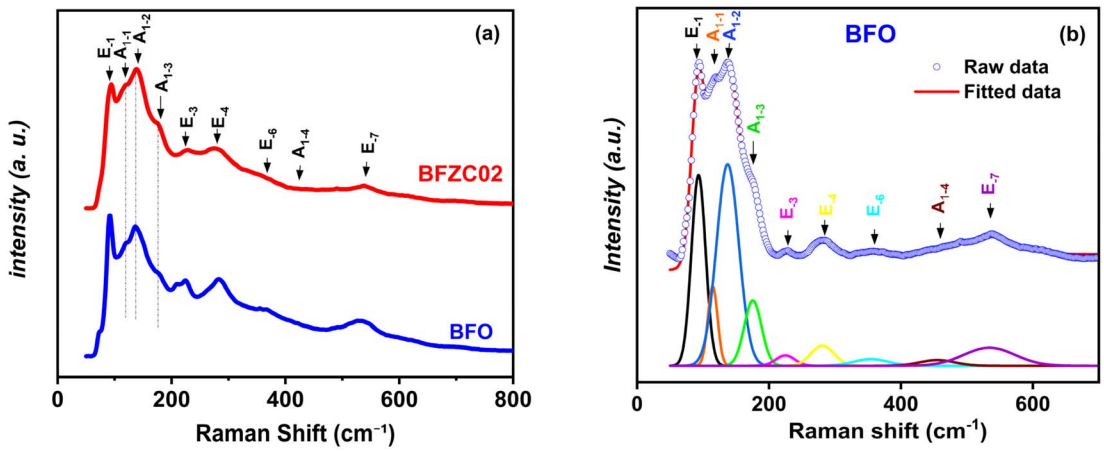

Fig. 3 Raman spectra of BFO and BFZC02 ceramics recorded at RT (a). Spectral deconvolution of BFO with the assignment of the corresponding vibrational modes (b).

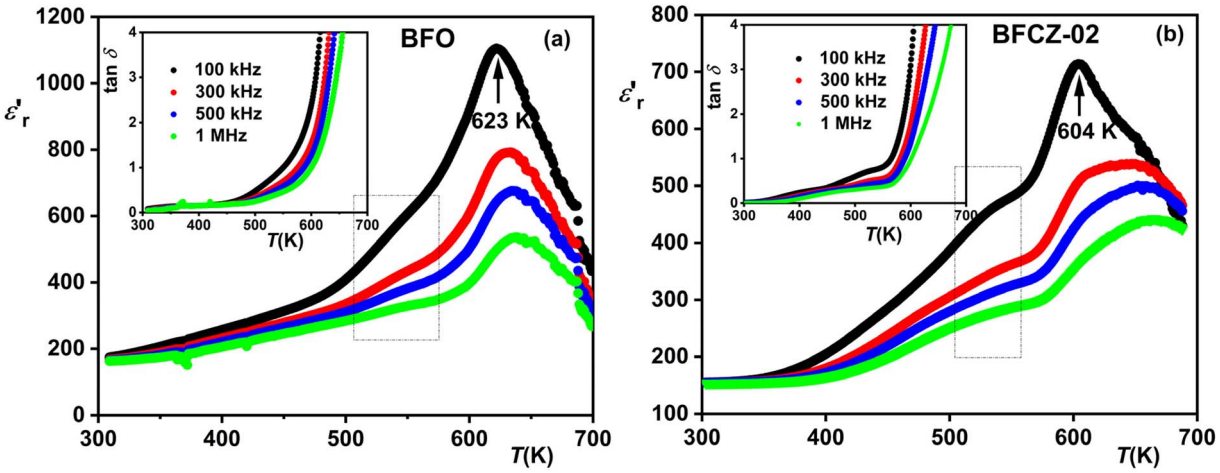

Fig. 4 $\varepsilon_r' = f(T)$ curves for BFO (a) and BFZC02(b) at different frequencies. The inset illustrates the corresponding $\tan\delta = f(T)$ curves for both compositions.

leads to the observed reduction in the Néel temperature of BFZC02. This interpretation is supported by the work of Durga *et al.*[33] Furthermore, the substitution not only reduces the Néel temperature (T_N) of BFO but also significantly lowers the tangent loss ($\tan\delta$) from approximately 0.080 (BFO, at RT and 100 kHz) to 0.011 for BFZC02, indicating improved dielectric quality as a result of co-substitution. This enhancement is likely due to the reduction of oxygen vacancies, as previously discussed in relation to the decrease in crystallite size following co-substitution. A similar reduction in $\tan\delta$ at RT was also observed when 2% Zr was doped into $Bi_{0.8}La_{0.2}FeO_3$.[34] The relative permittivity (ε_r') also decreases with substitution, dropping from 175 (BFO) to 155 (BFZC02) at RT and 100 kHz. This decline is likely due to partial clamping of domain wall motion, attributed to increased internal strain induced by doping, as indicated by the XRD study.[35,36]

On the other hand and just below T_N, an anomaly is observed for BFO, which becomes more pronounced and noticeable for BFZC02 (as highlighted within a rectangle in Fig. 4). According to Salah *et al.*,[37] this anomaly is due to the ordering of electric dipoles in the material, influenced by the electric field associated with the applied frequency. This effect is more significant following co-substitution with zirconium and copper.

3.4 Optical properties

The optical properties of the synthesized BFO and BFZC02 ceramics were investigated using UV-vis spectroscopy. Fig. 5 illustrates the absorption spectraof these ceramics in the wavelength range of 400 to 800 nm. In this region, an absorption peak is observed in the wavelength range of 400 to 440 nm for both prepared compounds, indicating that the band gap (E_g) lies within the visible region. To study the optical properties of BFO and BFZC02 ceramics, E_g was estimated using the classical Tauc relationship, expressed by the following equation:

$$\alpha h\nu = A(h\nu - E_g)^n \quad (5)$$

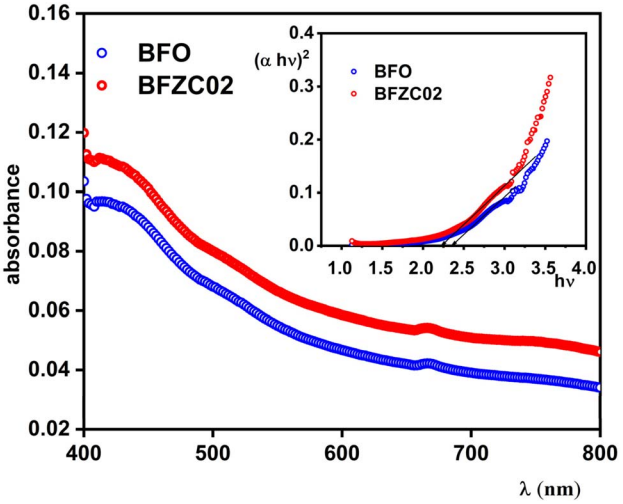

Fig. 5 UV-vis absorption spectra for BFO and BFZC02. The inset shows the plot of $(h\nu)^2$ as a function of $h\nu$ for both ceramics.

In this formula, A is a constant, $h\nu$ represents the photon energy, α is the absorption coefficient, and n depends on the type of electronic transition. The exponent n takes the value 1/2 for direct bandgap transitions and 2 for indirect transitions. According to previous studies,[38–41] BFO is known to exhibit a direct bandgap, and thus, we used $n = 1/2$ for our calculations. Here E_g represents the energy difference between the valence band maximum (O 2p) and the conduction band minimum (Fe 3d).[42] The absorption coefficient (α) is calculated using the Kubelka–Munk function:

$$\alpha = F(R) = \frac{(1-R)^2}{2R} \quad (6)$$

where R is the reflectance. From this perspective, we have plotted the variation of $(\alpha h\nu)^2$ as a function of $h\nu$ for BFO and BFZC02 in the inset of Fig. 5. The intersection of the extrapolation of the linear fit with the x-axis $[(\alpha h\nu)^2 = 0]$ allows us to

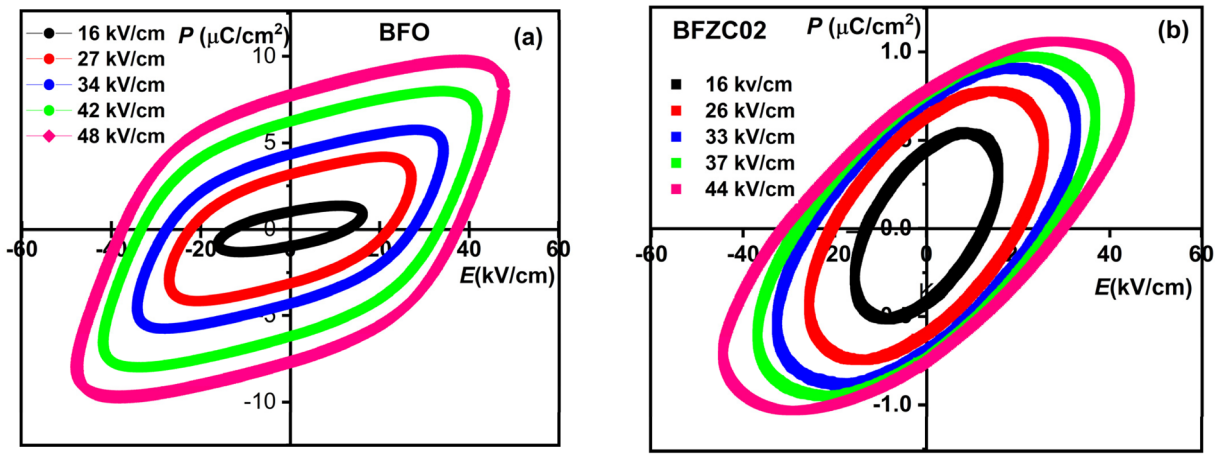

Fig. 6 $P = f(E)$ loops for BFO (a) and BFZC02 (b) in different applied fields and at room temperature.

determine the corresponding band gap value. The found values for E_g are 2.34 eV for BFO and 2.21 eV for BFZC02. This result demonstrates the significance of substituting Fe^{3+} with Zr^{4+} and Cu^{2+} in reducing the band gap energy of BFO. The reduction in the band gap leads to enhanced absorption across a larger portion of the solar spectrum, particularly in the visible range.

In the next step, we attempt to detail some reasons that have led to the decrease in the energy of the band gap following the co-substitution with Cu^{2+} and Zr^{4+}. The substitution with Cu^{2+} can result in a reduction of the band gap width. Indeed, Cu^{2+} has a lower conduction band edge energy level ($E_{cb} = -4.96$ eV) compared to Fe^{3+} ($E_{cb} = -4.78$ eV),[43] which could narrow the effective optical band gap between the O 2p valence band and the Fe 3d conduction band. This interpretation is supported by the work of M. Hasan *et al.*,[44] where they demonstrated that the substitution of Fe^{3+} with manganese Mn^{4+} ($E_{cb} = -5.83$ eV) reduced the band gap width of BFO. On the other hand, unlike metallic dopants, non-metallic ions such as Zr are less prone to generating donor levels in the band gap. Zr is capable of shifting the maximum of the valence band to higher energies. This deduction is supported by the work of Chen *et al.*[45] Similar reductions in E_g have been observed in Zr-doped BFO, as seen in BFO doped with Co[46] and BFO doped with Mn.[47] Consequently, the reduced E_g in the BFZC02 ceramic making it more suitable for photocatalytic and photovoltaic applications under visible-light illumination.

3.5 The *P–E* hysteresis loop study

The polarization hysteresis (*P–E*) loops of BFO (a) and BFZC02 (b), measured at RT, are presented in Fig. 6. The *P–E* loops for each composition are displayed under different applied electric fields. From these figures, it is evident that both pristine BFO and BFZC02 exhibit typical ferroelectric behavior, with well-defined hysteresis loops. However, the substitution of copper and zirconium results in more rounded *P–E* loops. The rounded shape of these loops suggests significant leakage current in BFZC02. This enhanced leakage current could arise from a reduction in the effective potential barrier height due to structural distortions caused by the co-substitution. This interpretation is supported by UV-vis spectrophotometry study, which reveal a decrease in the band gap of BFO (2.34 eV) with Cu and Zr substitution, resulting in a narrower band gap for BFZC02 (2.21 eV). This finding is consistent with previous work on Eu-doped BFO.[48] In the same study, we observe that the remanent polarization decreases with the co-substitution. Substituting Fe^{3+} with a small amount (2%) of slightly larger ions such as Zr^{4+} and Cu^{2+} can enhance charge hopping between Fe^{3+} and Fe^{2+} ions. This mechanism may explain the reduced ferroelectric character of BFO after co-doping, consistent with the work of S. Divya Lakshmi *et al.*.[49] Similarly, a pronounced reduction in remanent polarization has been observed in the Dy-doped $BiFe_{0.98}Cu_{0.02}O_3$ system,[50] where the polarization dropped from 125 μC cm^{-2} in undoped BFO to 0.28 μC cm^{-2} at a doping level of 1%. Despite this reduction, BFZC02 still maintains a significant ferroelectric response, indicating its potential for use in ferroelectric memory devices and sensors.

4 Conclusion

In this study, our objective is to enhance the optical and dielectric properties of BFO to make it suitable for advanced electronic and photovoltaic devices. To achieve this, we co-substitution the Fe-site with Cu^{2+} and Zr^{4+} at a very low concentration (2%), forming the compound $BiFe_{0.98}(Zr_{1/2}Cu_{1/2})_{0.02}O_3$ (BFCZ02). XRD analysis confirms the successful incorporation of Cu^{2+} and Zr^{4+} into the Fe-site lattice of BFO. Both XRD and Raman investigations demonstrate that the co-substitution does not alter the *R3c* structure of BFO. Moreover, the XRD study reveals a reduction in the formation of the secondary phase (selenite $Bi_{25}FeO_{39}$) and a significant decrease in crystallite size. Dielectric measurements revealed that the anomaly associated with the Néel temperature (T_N) in pure BFO, observed at 623 K, decreased significantly to 604 K in BFCZ02. This shift is attributed not to bond-angle distortions but to lowering the overall magnetic interaction strength *J*. In addition, the co-substitution reduced the optical bandgap from 2.34 eV for pure BFO to 2.21 eV for BFCZ02, enhancing its

absorption in the visible light range. This narrowing of the bandgap renders BFCZ02 a highly promising material for photocatalytic applications and solar energy conversion technologies. However, the reduction in bandgap energy (E_g) was observed to influence the saturation behavior of the polarization-electric field (P–E) hysteresis loops in BFCZ02, suggesting a trade-off between optical tunability and ferroelectric performance.

Author contributions

All authors contributed to the preparation of this manuscript. Material synthesis and data collection were carried out by S. Zaidi. Data analysis was conducted in collaboration between Z. Abdelkafi and H. Khemakhem. The initial draft of the manuscript was written by S. Zaidi in collaboration with Z. Abdelkafi, and all authors provided comments on previous versions of the manuscript. All authors read and approved the final version of the manuscript.

Conflicts of interest

The authors declare that they have no conflict of interest.

Data availability

The data supporting the findings of this study are available from the corresponding author upon reasonable request. No external repositories were used.

Acknowledgements

The authors acknowledge the Laboratory of Multifunctional Materials and Applications (LaMMA), (LR16ES18), Faculty of Sciences of Sfax, University of Sfax, (Tunisia).

References

1 S. Wang, H. Liu, Y. Wang, H. Qin, J. Zhao, Z. Lu, Z. Mao and D. Wang, *J. Am. Ceram. Soc.*, 2024, **107**, 205–213.
2 J. Zhang, Y. Pu, Y. Hao, Y. Yang, L. Zhang, B. Wang and Q. Pan, *J. Energy Storage*, 2025, **105**, 114786.
3 P. Fischer, M. Polomska, I. Sosnowska and M. Szymanski, *J. Phys. C: Solid State Phys.*, 1980, **13**, 1931.
4 C. Michel, J.-M. Moreau, G. D. Achenbach, R. Gerson and W. J. James, *Solid State Commun.*, 1969, **7**, 701–704.
5 W. Kaczmarek, Z. Pająk and M. Połomska, *Solid State Commun.*, 1975, **17**, 807–810.
6 V. R. Palkar, J. John and R. Pinto, *Appl. Phys. Lett.*, 2002, **80**, 1628–1630.
7 M. Boukhari, Z. Abdelkafi, N. Abdelmoula, H. Khemakhem and N. Randrianantoandro, *J. Mater. Sci.: Mater. Electron.*, 2023, **34**, 1218.
8 P. Chandra Sati, M. Arora, S. Chauhan, S. Chhoker and M. Kumar, *J. Appl. Phys.*, 2012, **112**, 094102.
9 S. Mukherjee, R. Gupta, A. Garg, V. Bansal and S. Bhargava, *J. Appl. Phys.*, 2010, **107**, 123535.
10 M. Kumar and K. L. Yadav, *J. Appl. Phys.*, 2006, **100**, 074111.
11 Y. Li, Y. Fan, H. Zhang, X. Teng, X. Dong, H. Liu, X. Ge, Q. Li, W. Chen, X. Li and Z. Ge, *J. Supercond. Novel Magn.*, 2014, **27**, 1239–1243.
12 M. Arora, S. Chauhan, P. C. Sati and M. Kumar, *J. Supercond. Novel Magn.*, 2014, **27**, 1867–1871.
13 W. Ben Taazayet, I. Mallek Zouari, P. Gemeiner, B. Dkhil and N. Thabet Mliki, *Phys. Status Solidi RRL*, 2022, **16**, 2200081.
14 R. D. Shannon, *Acta Crystallogr., Sect. A*, 1976, **32**, 751–767.
15 T. D. Rao and S. Asthana, *J. Appl. Phys.*, 2014, **116**, 164102.
16 R. Wegdan and G. Arunava, *J. Nanosci. Nanotechnol.*, 2018, **18**, 7804–7810.
17 J. Rodriguez-Carvajal, *Program FullProf (Version February 2019) Laboratoire Léon Brillouin*, CEA-CNRS, LLB-LCSIM 2019.
18 M. K. Anupama, B. Rudraswamy and N. Dhananjaya, *J. Alloys Compd.*, 2017, **706**, 554–561.
19 P. Mallick, S. K. Satpathy and B. Behera, *Bull. Mater. Sci.*, 2022, **45**, 198.
20 K. M. Batoo, G. Kumar, Y. Yang, Y. Al-Douri, M. Singh, R. B. Jotania and A. Imran, *J. Alloys Compd.*, 2017, **726**, 179–186.
21 A. Puhan, B. Bhushan, V. Kumar, H. S. Panda, A. Priyam, D. Das and D. Rout, *J. Mater. Sci. Eng. B*, 2019, **241**, 48–54.
22 S. Rani, O. Singh, S. Kaushik, P. Sharma, A. Agarwal and S. Sanghi, *J. Mater. Sci.: Mater. Electron.*, 2023, **34**, 258.
23 S. Chauhan, M. Arora, P. C. Sati, S. Chhoker, S. C. Katyal and M. Kumar, *Ceram. Int.*, 2013, **39**, 6399–6405.
24 D. Do, J. W. Kim and S. S. Kim, *J. Am. Ceram. Soc.*, 2011, **94**, 2792–2795.
25 R. Haumont, J. Kreisel, P. Bouvier and F. Hippert, *Phys. Rev. B:Condens. Matter Mater. Phys.*, 2006, **73**, 132101.
26 T. K. Pani, B. Sundaray, G. Sahoo and D. Rout, *J. Phys. D: Appl. Phys.*, 2020, **53**, 325001.
27 A. Puhan, B. Bhushan, V. Kumar, H. S. Panda, A. Priyam, D. Das and D. Rout, *J. Mater. Sci. Eng. B*, 2019, **241**, 48–54.
28 P. Hermet, M. Goffinet, J. Kreisel and Ph. Ghosez, *Phys. Rev. B:Condens. Matter Mater. Phys.*, 2007, **75**, 220102.
29 M. Arora, S. Chauhan, P. C. Sati, M. Kumar, S. Chhoker and R. K. Kotnal, *J. Mater. Sci.: Mater. Electron.*, 2014, **25**, 4286–4299.
30 H. Singh and K. L. Yadav, *Ceram. Int.*, 2015, **41**, 9285–9295.
31 G. Khasskhoussi, Z. Abdelkafi, H. Khelifi, N. Abdelmoula, D. Mezzane and H. Khemakhem, *J. Alloys Compd.*, 2017, **701**, 43–48.
32 P. Chandra Sati, M. Kumar and S. Chhoker, *Ceram. Int.*, 2015, **41**, 3227–3236.
33 T. Durga Rao and S. Asthana, *J. Appl. Phys.*, 2014, **116**, 164102.
34 H. M. Usama, A. Sharif, M. A. Zubair, M. A. Gafur and S. M. Hoque, *J. Appl. Phys.*, 2016, **120**, 214106.
35 Ja. Dhahri, M. Boudard, S. Zemni, H. Roussel and M. Oumezzine, *J. Solid State Chem.*, 2008, **181**, 802–811.
36 S. Riaz, S. M. H. Shah, A. Akbar, S. Atiq and S. Naseem, *J. Sol-Gel Sci. Technol.*, 2015, **74**, 329–339.
37 M. Salah, I. Morad, H. E. Ali, M. M. Mostafa and M. M. El-Desoky, *J. Inorg. Organomet. Polym.*, 2021, **31**, 3700–3710.

38 P. R. Vanga, R. V. Mangalaraja and M. Ashok, *Mater. Res. Bull.*, 2015, **72**, 299–305.
39 J. F. Ihlefeld, N. J. Podraza, Z. K. Liu, R. C. Rai, X. Xu, T. Heeg, Y. B. Chen, J. Li, R. W. Collins, J. L. Musfeldt, X. Q. Pan, J. Schubert, R. Ramesh and D. G. Schlom, *Appl. Phys. Lett.*, 2008, **92**, 142908.
40 Y. Xu and M. Shen, *Mater. Lett.*, 2008, **62**, 3600–3602.
41 A. Manzoor, A. M. Afzal, N. Amin, M. I. Arshad, M. Usman, M. N. Rasool and M. F. Khan, *Ceram. Int.*, 2016, **42**, 11447–11452.
42 M. Hasan, M. A. Basith, M. A. Zubair, Md. S. Hossain, R. Mahbub, M. A. Hakim and Md. F. Islam, *J. Alloys Compd.*, 2016, **687**, 701–706.
43 Y. Xu and M. A. A. Schoonen, *Am. Mineral.*, 2000, **85**, 543–556.
44 M. Hasan, M. A. Basith, M. A. Zubair, Md. S. Hossain, R. Mahbub, M. A. Hakim and Md. F. Islam, *J. Alloys Compd.*, 2016, **687**, 701–706.
45 X. Chen, S. Shen, L. Guo and S. S. Mao, *Chem. Rev.*, 2010, **110**, 6503–6570.
46 Z. Li, L. Cheng, S. Zhang, Z. Wang and C. Fu, *J. Solid State Chem.*, 2019, **279**, 120978.
47 M. Abushad, W. Khan, S. Naseem, S. Husain, M. Nadeem and A. Ansari, *Ceram. Int.*, 2019, **45**, 7437–7445.
48 T. Durga Rao, R. Ranjith and S. Asthana, *J. Appl. Phys.*, 2014, **115**, 124110.
49 S. D. Lakshmi, I. B. S. Banu, R. Rajesh, M. H. Mamat and G. Gowri, *Appl. Phys. A*, 2023, **129**, 552.
50 A. S. Priya, I. B. S. Banu and S. Anwar, *J. Magn. Magn. Mater.*, 2016, **401**, 333–338.